[논 문] 한국재료학회지
Korean J. Mater. Res.
Vol. 34, No. 8 (2024)

https://doi.org/10.3740/MRSK.2024.34.8.387

Hydrated Vanadium Pentoxide/Graphene Oxide Nanobelts for Enhanced Electrochemical Performance

Hyegyeong Hwang[1] and Jinsung Kwak[2†]

[1]Department of Materials Convergence and System Engineering, Changwon National University, Changwon 51140, Republic of Korea
[2]Department of Physics & Department of Materials Convergence and System Engineering, Changwon National University, Changwon 51140, Republic of Korea

(Received July 22, 2024 : Revised August 10, 2024 : Accepted August 14, 2024)

Abstract Transition metal oxide-based materials have mainly been studied as electrodes for energy storage devices designed to meet essential energy demands. Among transition metal oxide-based materials, hydrated vanadium pentoxide ($V_2O_5 \cdot nH_2O$), a vanadium oxide material, has demonstrated great electrochemical performance in the electrodes of energy storage devices. Graphene oxide (GO), a carbon-based material with high surface area and high electrical conductivity, has been added to $V_2O_5 \cdot nH_2O$ to compensate for its low electrical conductivity and structural instability. Here, $V_2O_5 \cdot nH_2O$/GO nanobelts are manufactured with water without adding acid to ensure that the GO is uniformly dispersed, using a microwave-assisted hydrothermal synthesis. The resulting $V_2O_5 \cdot nH_2O$/GO nanobelts exhibited a high specific capacitance of 206 F/g and more stable cycling performance than $V_2O_5 \cdot nH_2O$ without GO. The drying conditions of the carbon paper electrodes also resulted in more stable cycling performance when conducted at high vacuum and high temperature, compared with low vacuum and room temperature conditions. The improvement in electrochemical performance due to the addition of GO and the drying conditions of carbon paper electrodes indicate their great potential value as electrodes in energy storage devices.

Key words $V_2O_5 \cdot nH_2O$/graphene oxide composite, nanobelts, microwave-assisted hydrothermal synthesis, electrochemical performance.

1. Introduction

Energy is essential in modern society, and research on energy storage devices is gradually increased in the requirement of energy. Energy storage devices such as batteries and supercapacitors have been used to satisfy the demand for electric vehicles, various electronic devices and supplies.[1-6] Supercapacitors, also called electrochemical capacitors, have outstanding electrochemical performance including high power density, fast charge/discharge kinetics, stable cycle performance and large specific capacitance etc.[7-9] Furthermore, supercapacitors comprise electrodes, electrolyte, separator and current collectors, which might relate to the electrochemical performance. Transition metal oxide-based electrode materials for supercapacitors, such as ruthenium oxide (RuO_2), manganese oxide (MnO_2), cobalt oxide (Co_3O_4), nickel oxide (NiO), copper oxide (CuO), molybdenum oxide (MoO_3), ferric oxide (Fe_2O_3) and vanadium oxide (V_2O_5), exhibit excellent electrochemical performance for attractive supercapacitive behaviors as high theoretical capacitance and high cycling stability.[10-17]

Among transition metal oxide-based electrode materials, vanadium oxide-based materials (V_2O_5, VO_2, V_2O_3, V_6O_{13} etc.) has been frequently investigated as electrodes of energy storage devices for several years and has mostly synthesized by adding acid to vanadium precursor.[17-20] Above all, the advantages of vanadium pentoxide (V_2O_5) are a layered structure, high theoretical specific capacitance, multiple oxi-

†Corresponding author
E-Mail : jkwak@changwon.ac.kr (J. Kwak, Changwon Nat'l Univ.)

© Materials Research Society of Korea, All rights reserved.
This is an Open-Access article distributed under the terms of the Creative Commons Attribution Non-Commercial License (https://creativecommons.org/licenses/by-nc/4.0/) which permits unrestricted non-commercial use, distribution, and reproduction in any medium, provided the original work is properly cited.

dation valence state, low cost and natural abundance.[21,22] In addition, hydrated vanadium pentoxide ($V_2O_5 \cdot nH_2O$) that H_2O inserted into V_2O_5 is expanded interlayer spacing of V_2O_5 material to improve electrochemical performance due to the expanded layered structure.[23] However, $V_2O_5 \cdot nH_2O$ and V_2O_5 have low electrical conductivity and structural instability which might restrict implementation of energy storage devices.[24-26] To solve these problems, $V_2O_5 \cdot nH_2O$ has been used along with carbon-based materials that substantial surface area and high electrical conductivity such as carbon nanotube (CNT), reduced graphene oxide (rGO) and graphene oxide (GO).[27-29] Geng and Wang[28] developed $V_2O_5 \cdot nH_2O$/graphene composite for supercapacitors that was greater electrochemical performance than $V_2O_5 \cdot nH_2O$ xerogel by adding GO. Fan et al.[29] reported $V_2O_5 \cdot nH_2O$/rGO composite film that $V_2O_5 \cdot nH_2O$ was sandwiched with rGO by chemical bonding to ensure good mechanical properties, which exhibited high specific capacitance and good cycling stability for ammonium-ion energy storage. In particular, abundant oxygen functional groups and high specific surface area of GO increase electrochemical performance.[30,31] Dai et al.[30] developed MnO_2 nanowires/GO nanosheets composite that possessed high specific capacitance and high cycle performance due to the oxygen functional groups and high specific surface area of GO, and the composite was prevented aggregation of GO and MnO_2 nanowires and accordingly provided high specific surface area. Additionally, electrochemical performance might vary according to various drying processes at pressure and temperature.[32] Azadvari et al.[32] reported MXene of a three-layered structure that had better electrochemical performance and higher capacitance retention under vacuum-drying condition at 80 °C than under air-drying condition at 25 °C.

Herein, we demonstrate that increase electrochemical performance of $V_2O_5 \cdot nH_2O$/GO nanobelts added with GO through a simple microwave-assisted hydrothermal synthesis. Moreover, we manufacture $V_2O_5 \cdot nH_2O$/GO nanobelts based on water without using acid. $V_2O_5 \cdot nH_2O$/GO nanobelts exhibit high specific capacitance of 206 F/g at 0.1 A/g and enhanced cycle stability, which is better than $V_2O_5 \cdot nH_2O$ that shows specific capacitance of 108 F/g at 0.1 A/g and low cycle stability. Also, we investigate differences in electrochemical performance of $V_2O_5 \cdot nH_2O$/GO nanobelts depending on drying processes of carbon paper electrode at different pressure and temperature. These electrochemical properties of $V_2O_5 \cdot nH_2O$/GO nanobelts become a potential candidate as an electrode for supercapacitors.

2. Experimental Procedure

$V_2O_5 \cdot nH_2O$/GO, the result of V_2O_5 and GO in water, was manufactured by mixing V_2O_5 powder (Sigma-Aldrich, item No. 223794), GO (CHARMGRAPHENE, 2 mg/mL), and DI water and then using a microwave-assisted hydrothermal method. 7 mg V_2O_5 was mixed in 15 mL water and stirred for 12 h using a magnetic bar, then stirred for 3 h at 50 °C. This solution was filtered using PVDF filter paper with a pore size of 0.22 μm. The filtered solution of 12 mL was added GO 0.1 mL and sonicated for 10 min. This solution was transferred to glass vial and reacted microwave-assisted hydrothermal process with stirring at 150 °C for 1 h. The product was vacuum filtered using the filter paper and washed with water. Additionally, $V_2O_5 \cdot nH_2O$ was prepared in the same process by excluding GO.

A mixture of completely reduced VO_2 and partially reduced $V_{10}O_{24} \cdot nH_2O$, a result of V_2O_5 in oxalic acid (Sigma-Aldrich, item No. 194131), was manufactured by mixing V_2O_5, water, and oxalic acid and then using a microwave-assisted hydrothermal method. 0.727 g V_2O_5 and 1.080 g oxalic acid were mixed in 72 mL water and stirred for 12 h using a magnetic bar. This solution was transferred to glass vial and reacted microwave-assisted hydrothermal process with stirring at 150 °C for 1 h.

The product was vacuum filtered using the filter paper and washed several times with water and ethanol.

The structural characterization of the results created by the above process was measured. The X-ray diffraction (XRD) patterns were obtained by an X-ray diffractometer (Rigaku, MiniFlex 600) using Cu-Kα radiation in the range of 3° to 60° (2θ) with scanning rate of 2°/min. The Raman spectra were measured by a Raman spectrometer (Thermo Fisher Scientific, DXR3xi) with laser excitation of 532 nm at power of 1 mW. The morphology was evaluated by a field emission scanning electron microscopy (FE-SEM; Tescan, CZ/MIRA I LMH).

A process was carried out to measure electrochemical properties as follows. 1 mg active material, 20 μL nafion, 200 μL ethanol and 800 μL water were mixed using ultra-

sonicator for 20 min. This solution of 30 μL was dropped on carbon paper and dried at different processes then the dried carbon papers were used the electrode. A drying process of the carbon paper, low-vacuum (500~760 torr) room temperature (RT) process, the carbon paper was dried in oven at 60 °C for 2 h and in low vacuum at RT for 12 h. Another drying process of the carbon paper, high-vacuum (10^{-3}~10^{-4} torr) 100 °C process, the carbon paper was dried in oven at 60 °C for 15 min and then dried in high vacuum at 100 °C for 2 h.

The electrochemical measurement was assessed by a three-electrode system using electrochemical workstation (Ivium Technologies, IviumStat.h). an Ag/AgCl electrode, a graphite rod and the active material on carbon paper were used as the reference electrode, the counter electrode and the working electrode. The electrolyte was used by 2 M KCl solution. The cyclic voltammetry (CV), galvanostatic charge-discharge (GCD) and electrochemical impedance spectroscopy (EIS) were executed. The voltage window for CV and GCD measurements was 0 to 0.8 V. The frequency range for EIS was from 100 kHz to 0.1 Hz with an amplitude of 5 mV. The specific capacitance (C_S, F/g) was calculated from CV curve and GCD curve by the following Eqs. (1) and (2).[33,34)]

$$C_S = \frac{\oint I(V)dV}{m \times v \times \Delta V} \tag{1}$$

where, $\oint I(V)dV$ is the integrated area of the CV curve, m (g) is the mass of active material on carbon paper, v (mV/s) is the scan rate, ΔV (V) is the potential window.

$$C_S = \frac{I\Delta t}{m\Delta V} \tag{2}$$

where, I (A) is the discharge current, Δt (s) is the discharge time, m (g) is the mass of active material on carbon paper, ΔV (V) is the potential change during discharge process.

3. Results and Discussion

The synthesis process of $V_2O_5 \cdot nH_2O$/GO nanobelts is shown in Fig. 1. V_2O_5 powder was dissolved in deionized water and filtered to make V_2O_5 solution with uniformly diffused V^{5+} ions. The V_2O_5 solution was mixed with GO and sonicated that completely dispersed. This solution formed $V_2O_5 \cdot nH_2O$/GO through microwave-assisted hydrothermal reaction. The result became a flexible paper using vacuum filtration. Vanadium oxide-materials including $V_2O_5 \cdot nH_2O$ were chiefly generated by adding acids (hydrogen peroxide, oxalic acid, citric acid, sulfuric acid etc.) to vanadium precursor.[35-41)] The resultant existed as a mixture in Fig. 1, VO_2 and $V_{10}O_{24} \cdot nH_2O$, when oxalic acid was added to V_2O_5

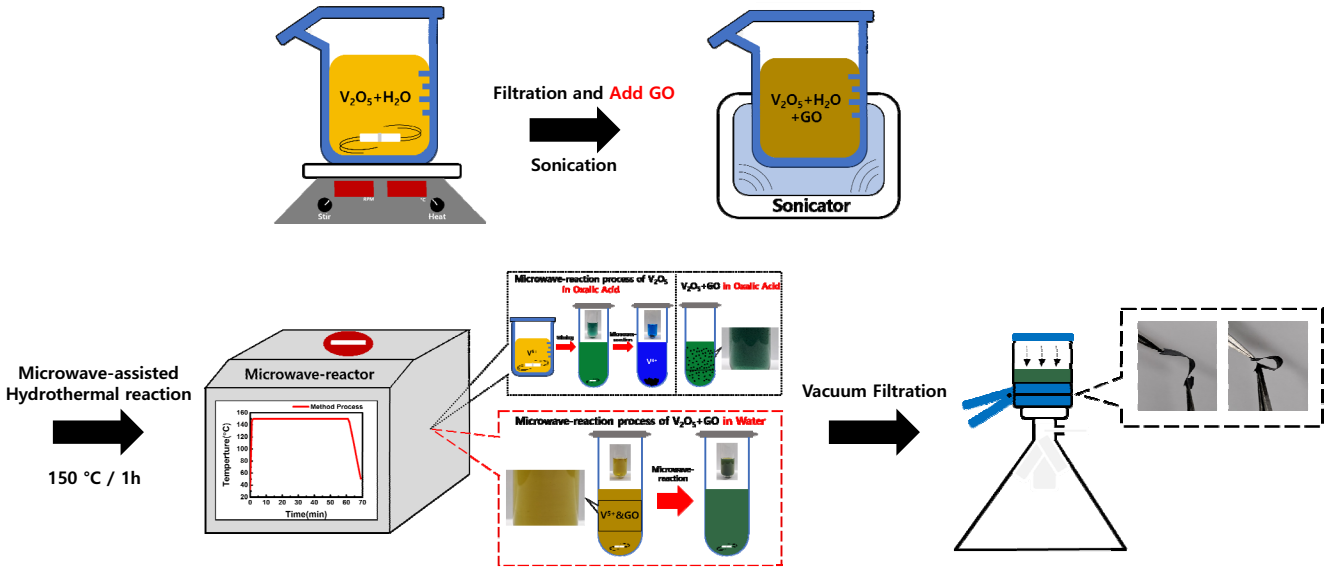

Fig. 1. Illustration on the preparation of $V_2O_5 \cdot nH_2O$/GO nanobelts. Image (left) of black dotted box is a mixture of completely reduced VO_2 and partially reduced $V_{10}O_{24} \cdot nH_2O$ after microwave-assisted hydrothermal reaction process of V_2O_5 in oxalic acid. Image (right) of black dotted box is not uniform diffusion of GO when V_2O_5 + GO in oxalic acid. In image of red dotted box, V^{5+} ions and GO are uniformly mixed by sonication and formed $V_2O_5 \cdot nH_2O$/GO nanobelts after microwave-assisted hydrothermal reaction process of V_2O_5 + GO in water.

powder and water. However, inset digital image (Fig. 1) and Fig. S1 show that GO cannot be dispersed in oxalic acid (pH 1). Because of the relationship between GO and pH, it was not completely dispersed in acid (pH 1), therefore it was likely that the effect of GO would not be applied uniformly.[42)]

Fig. 2(a) shows characteristic diffraction peaks that V_2O_5 has different results in water and oxalic acid after microwave-assisted hydrothermal reaction. Si/SiO_2 substrate was used to support the results and the substrate peak is observed in the XRD pattern. The XRD pattern of V_2O_5 in oxalic acid shows as the mixture that exists completely reduced VO_2 and partially reduced $V_{10}O_{24} \cdot nH_2O$. VO_2 is completely reduced from V^{5+} to V^{4+}. The reduction reaction of VO_2 using V_2O_5 and oxalic acid is described by following Eqs. (3) and (4).[43)]

$$V_2O_5 + 3H_2C_2O_4 \rightarrow XOC_2O_4 + 2CO_2 + 3H_2O \quad (3)$$

$$VOC_2O_4 \rightarrow VO_2 + CO_2 + CO \quad (4)$$

However, due to a low temperature process condition of 150 °C or soft-reducing condition, V^{5+} is partially reduced to produce $V_{10}O_{24} \cdot nH_2O$.[44,45)] The XRD pattern confirms that is included $V_{10}O_{24} \cdot nH_2O$ (JCPDS No. 00-025-1006) among the peaks of VO_2 (JCPDS No. 01-084-3056). The XRD pattern of V_2O_5 in water shows which is not reduced from V^{5+}. Compared with XRD analysis of V_2O_5 powder (Fig. S2), H_2O is inserted into V_2O_5 to become $V_2O_5 \cdot nH_2O$ (JCPDS No. 00-040-1296) after microwave-assisted hydrothermal reaction. Fig. 2(b) displays Raman analysis to identify structures of vanadium oxide. $V_2O_5 \cdot nH_2O$ has vibration modes of chemical bond related to vanadium and oxide in 50~1,100 cm^{-1}. The bands at 89 cm^{-1} and 156 cm^{-1} in low-frequency mode are assigned to the lattice vibration with layered structure.[46,47)] The V=O bending mode is observed at 266 cm^{-1} and 407 cm^{-1}.[48)] The bands at 316 cm^{-1} corresponds to the V_3-O bending modes.[49)] The band at 503 cm^{-1} is assigned to the stretching mode of the V_3-O mode.[48)] The stretching mode of V_2-O is observed at 692 cm^{-1}.[46)] The stretching mode of V=O is located at 1,012 cm^{-1}.[48)] During microwave-assisted hydrothermal reaction, water molecules are inserted between V_2O_5 layers to intense peak of 503 cm^{-1} and 692 cm^{-1}.[50)] The Raman analysis of $V_2O_5 \cdot nH_2O/GO$ also shows chemical bonds related to V-O type and is similar to $V_2O_5 \cdot nH_2O$ in 50~1,100 cm^{-1}. In the inset image of Fig. 2(b), $V_2O_5 \cdot nH_2O/GO$ has D peak and G peak that demonstrate the existence of carbon materials in 1,200~1,800 cm^{-1}. The G peak at 1,600 cm^{-1}, representing the E_{2g} mode, is shifted due to oxygenation.[51)] In addition, the reduction in size of in plane sp^2

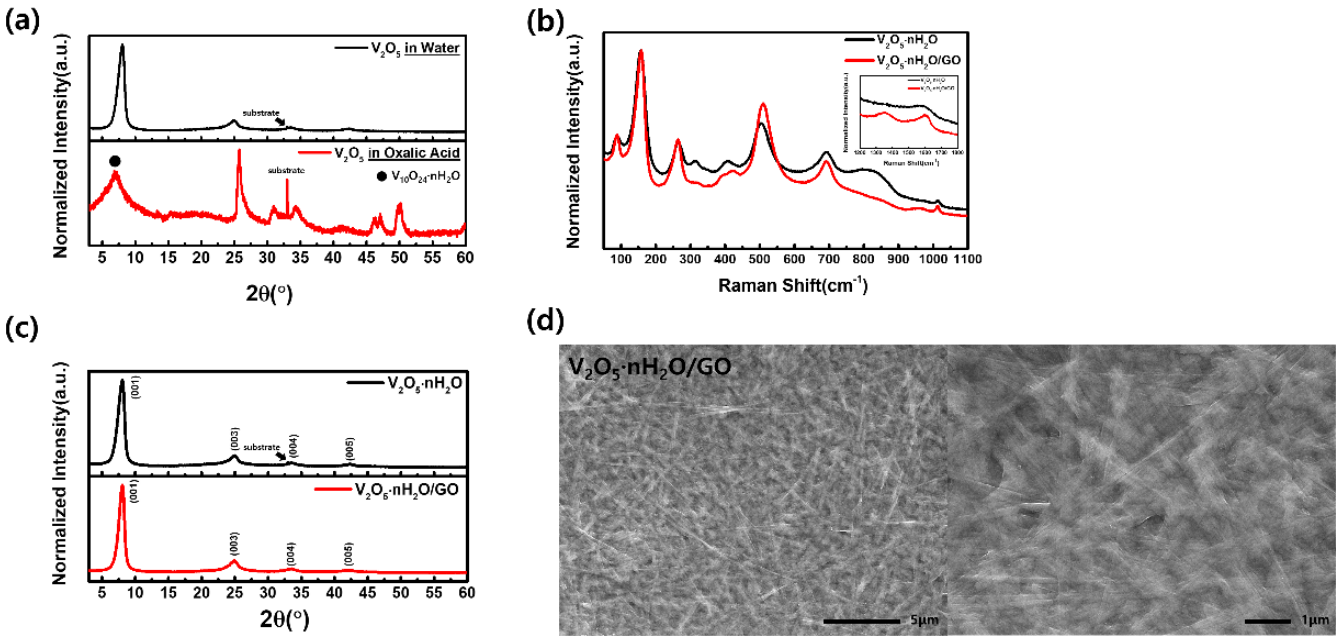

Fig. 2. (a) XRD patterns of V_2O_5 in water and oxalic acid on substrate after microwave-assisted hydrothermal reaction. (b) Raman spectra of $V_2O_5 \cdot nH_2O$ and $V_2O_5 \cdot nH_2O/GO$ on substrate. (c) XRD patterns of $V_2O_5 \cdot nH_2O$ and $V_2O_5 \cdot nH_2O/GO$ on substrate. (d) SEM image of $V_2O_5 \cdot nH_2O/GO$.

domains in graphite after oxidation, resulting in a broadened D peak at 1,353 cm^{-1}.[52] Fig. 2(c) shows $V_2O_5 \cdot nH_2O/GO$ and $V_2O_5 \cdot nH_2O$ which correspond to (001), (003), (004), (005) lattice plane. These planes confirm a layered structure of $V_2O_5 \cdot nH_2O$ (JCPDS No. 00-040-1296). The characteristic peaks of $V_2O_5 \cdot nH_2O/GO$ and $V_2O_5 \cdot nH_2O$ comprise similar peak positions, which means that GO not affect the lattice position. Si/SiO_2 substrate peak is observed in the XRD pattern. As displayed in Fig. 2(d) and Fig. S3, $V_2O_5 \cdot nH_2O/GO$ and $V_2O_5 \cdot nH_2O$ exhibit a nanobelt-like morphology. However, unlike $V_2O_5 \cdot nH_2O$ in Fig. S3, $V_2O_5 \cdot nH_2O/GO$ in Fig. 2(d) shows a clear nanobelt morphology due to likely prevented aggregation of GO and $V_2O_5 \cdot nH_2O$.[30,31]

Fig. 3(a) displays the CV curves of $V_2O_5 \cdot nH_2O/GO$ and $V_2O_5 \cdot nH_2O$ between 0 and 0.8 V at a scan rate of 100 mV/s. Fig. 3(a) shows the scan rate of 100 mV/s among the CV curves at different scan rates which measured in order from 5 mV/s to 100 mV/s in Fig. S4(a, b). When comparing the integrated area under CV curves, specific capacitance is larger in $V_2O_5 \cdot nH_2O/GO$. Therefore, the calculated specific capacitance of $V_2O_5 \cdot nH_2O$ and $V_2O_5 \cdot nH_2O/GO$ at a scan rate of 100 mV/s is 127.58 F/g and 350.86 F/g. Fig. 3(b, c) indicate the GCD curves at various current densities of $V_2O_5 \cdot nH_2O/GO$ and $V_2O_5 \cdot nH_2O$. As shown in Fig. 3(d), the GCD curves at various current densities of $V_2O_5 \cdot nH_2O/GO$ and $V_2O_5 \cdot nH_2O$ are manifested as the calculated specific capacitance. The specific capacitance of $V_2O_5 \cdot nH_2O/GO$ is 206, 182, 170, 160 F/g under current density of 0.1, 0.5, 1, 2 A/g. The specific capacitance of $V_2O_5 \cdot nH_2O$ is 108, 86, 75, 65 F/g under current density of 0.1, 0.5, 1, 2 A/g. Accordingly, $V_2O_5 \cdot nH_2O/GO$ under the same measuring conditions has greater specific capacitance than $V_2O_5 \cdot nH_2O$ due to abundant oxygen functional groups and high specific surface area of GO.[30,31]

The Nyquist plots of $V_2O_5 \cdot nH_2O/GO$ and $V_2O_5 \cdot nH_2O$ from 100 kHz to 0.1 Hz frequency region are presented in Fig. 4(a) and based on the equivalent circuit of Fig. S5. $V_2O_5 \cdot nH_2O/GO$ in Fig. 4(a) shows larger slope of the sloping line in low frequency region than $V_2O_5 \cdot nH_2O$ that indicates the fast diffusion rate of ions.[53] Moreover, Fig. 4(b) shows the

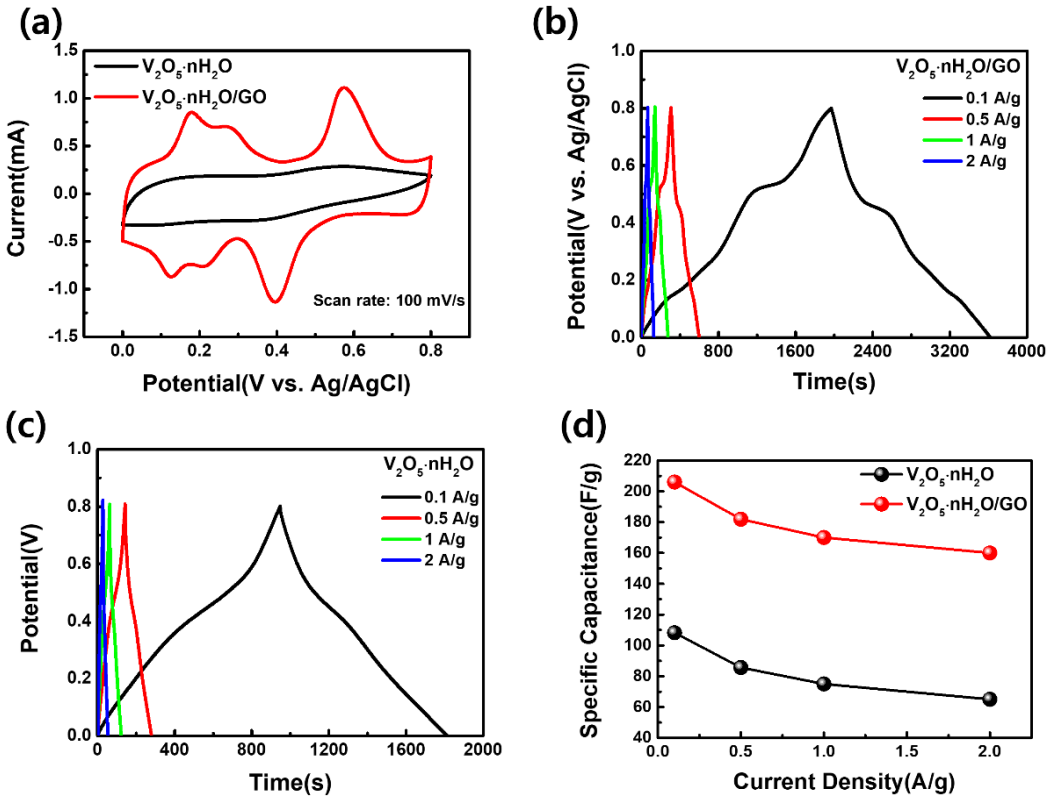

Fig. 3. (a) CV curves of $V_2O_5 \cdot nH_2O/GO$ and $V_2O_5 \cdot nH_2O$ at scan rate of 100 mV/s. (b) GCD curves of $V_2O_5 \cdot nH_2O/GO$ at different current densities. (c) GCD curves of $V_2O_5 \cdot nH_2O$ at different current densities. (d) Specific capacitance versus current density of $V_2O_5 \cdot nH_2O/GO$ and $V_2O_5 \cdot nH_2O$.

Nyquist plots at high frequency region. The diameter of semicircle in Fig. 4(b) implies charge transfer resistance (R_{ct}), the electrode resistance, which is associated to the surface area and conductivity of the electrode.[54] The R_{ct} values of $V_2O_5 \cdot nH_2O$/GO and $V_2O_5 \cdot nH_2O$ are 6.0 Ω and 20.2 Ω. The low resistance value of $V_2O_5 \cdot nH_2O$/GO is due to the inclusion of GO that features high conductivity and high surface area.[55] Additionally, the low resistance value of $V_2O_5 \cdot nH_2O$/GO exhibits a fast electrochemical reaction.[56] Fig. 4(c) shows the cycling performances of $V_2O_5 \cdot nH_2O$/GO and $V_2O_5 \cdot nH_2O$ during 200 cycles and 100 cycles at scan rate of 100 mV/s. Cycling performance of $V_2O_5 \cdot nH_2O$ has specific capacitance retention rate of 57.26 % in 100 cycles. Cycling performance of $V_2O_5 \cdot nH_2O$/GO has specific capacitance retention rate of 85.91 % in 100 cycles and 73.84 % in 200 cycles. $V_2O_5 \cdot nH_2O$/GO indicates better cycling performance than $V_2O_5 \cdot nH_2O$, which is due to GO possesses high specific surface area and abundant oxygen functional group.[30,31] Fig. 4(d) shows cycling performances depending on the drying processes. The high-vacuum 100 °C process and the low-vacuum RT process have capacitance retention of 81.65 % and 73.84 % at 200 cycles. The high-vacuum 100 °C process has better cycling performance than the low-vacuum RT process due to the drying process at high vacuum and high temperature.[32] In addition, Fig. S6, the initial cycle curves of cycling performance in Fig. 4(d) at different drying processes, has specific capacitance of 388.4 F/g in the high-vacuum 100 °C process and the specific capacitance (388.4 F/g) greater than specific capacitance of 385.08 F/g in the low-vacuum RT process.

4. Conclusion

$V_2O_5 \cdot nH_2O$/GO nanobelts were fabricated through microwave-assisted hydrothermal reaction by utilizing V_2O_5, water and GO. The structural properties of $V_2O_5 \cdot nH_2O$/GO nanobelts that produced after the reaction were confirmed through XRD analysis, Raman analysis and SEM image. The electrochemical properties of $V_2O_5 \cdot nH_2O$/GO nanobelts present high specific capacitance of 206 F/g at 0.1 A/g and stable cycling performance. $V_2O_5 \cdot nH_2O$/GO nanobelts exhibit higher specific capacitance, cycling performance, lower charge

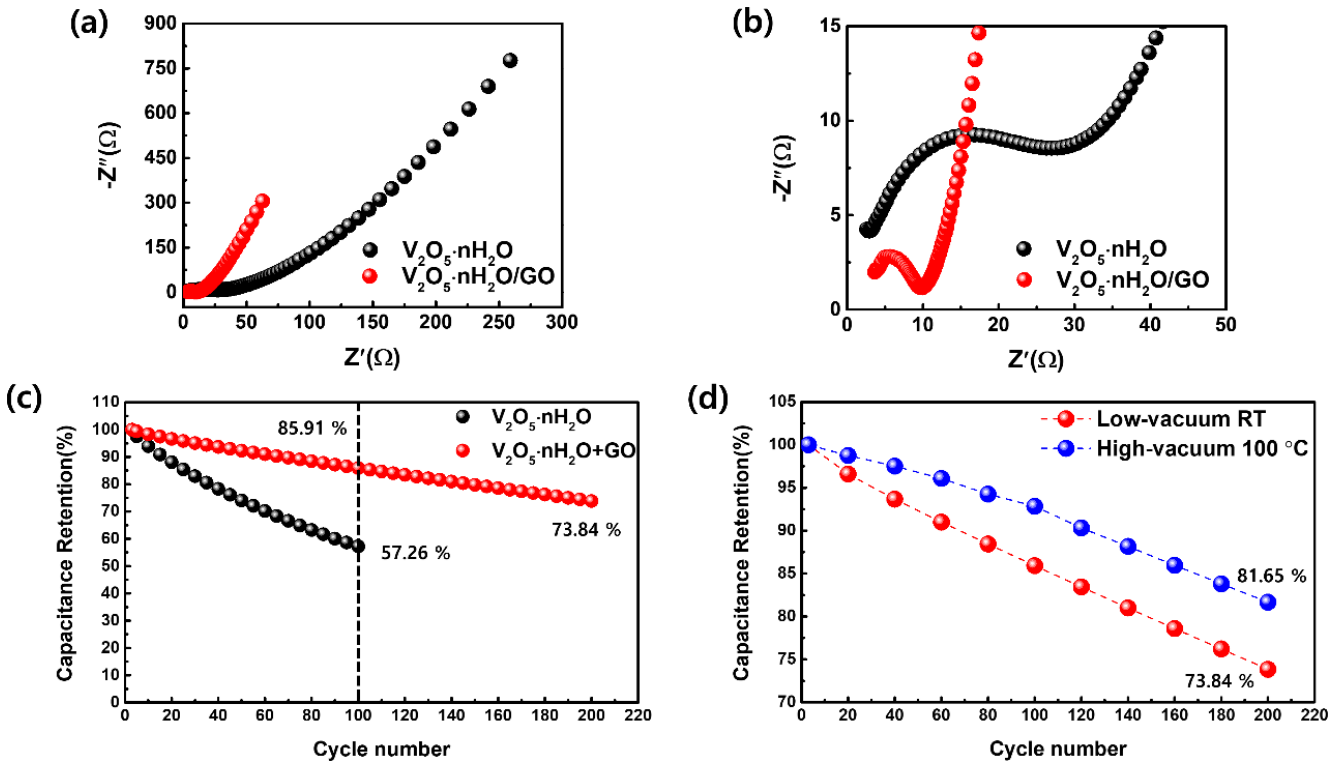

Fig. 4. (a) Nyquist plots of $V_2O_5 \cdot nH_2O$/GO and $V_2O_5 \cdot nH_2O$ from 0.1 Hz to 100 MHz region. (b) Nyquist plots of $V_2O_5 \cdot nH_2O$/GO and $V_2O_5 \cdot nH_2O$ in high-frequency region. (c) Cycling performances of $V_2O_5 \cdot nH_2O$/GO and $V_2O_5 \cdot nH_2O$ during 200 cycles at scan rate of 100 mV/s. (d) Cycling performances of $V_2O_5 \cdot nH_2O$/GO at different vacuum and temperature conditions in scan rate of 100 mV/s.

transfer resistance and faster ion diffusion rate than $V_2O_5 \cdot nH_2O$. In addition to using GO, $V_2O_5 \cdot nH_2O$/GO nanobelts indicate great specific capacitance and cycling performance by drying at high vacuum and high temperature. These good electrochemical performances of $V_2O_5 \cdot nH_2O$/GO nanobelts exhibit a great potential as an energy storage device electrode.

Availability of Data and Materials

All data generated or analyzed during this study are included in this published article and supplementary information.

Acknowledgement

This research was funded by the 'Lecturer-Graduate Student-Faculty Collaboration Research Project' at Changwon National University in 2024.

References

1. F. M. N. U. Khan, M. G. Rasul, A. S. M. Sayem and N. K. Mandal, J. Energy Storage, **71**, 108033 (2023).
2. D. Lemian and F. Bode, Energies, **15**, 5683 (2022).
3. J. Li, P. Ruan, X. Chen, S. Lei, B. Lu, Z. Chen and J. Zhou, ACS Energy Lett., **8**, 2904 (2023).
4. M. Weng, J. Zhou, Y. Ye, H. Qiu, P. Zhou, Z. Luo and Q. Guo, J. Colloid Interface Sci., **647**, 277 (2023).
5. S. Patel, A. Ghosh and P. K. Ray, J. Energy Storage, **73**, 109082 (2023).
6. L. Wei, S. T. Liu, M. Balaish, Z. Li, X. Y. Zhou, J. L. Rupp and X. Guo, Mater. Today, **58**, 297 (2022).
7. R. R. Zhang, Y. M. Xu, D. Harrison, J. Fyson, F. L. Qiu and D. Southee, Int. J. Autom. Comput., **12**, 43 (2015).
8. X. Huang, Y. Huang, G. Xu and X. Wang, J. Power Sources, **581**, 233488 (2023).
9. M. Manikandan, K. Subramani, M. Sathish and S. Dhanuskodi, ChemistrySelect, **3**, 9034 (2018).
10. B. Nisha, Y. Vidyalakshmi and S. A. Razack, Adv. Powder Technol., **31**, 1001 (2020).
11. Y. Yuan, J. Zhu, Y. Wang, S. Li, P. Jin and Y. Chen, J. Alloys Compd., **830**, 154524 (2020).
12. L. Kunhikrishnan and R. Shanmugham, Mater. Charact., **177**, 111160 (2021).
13. A. Ali, M. Ammar, A. Mukhtar, T. Ahmed, M. Ali, M. Waqas, M. N. Amin and A. Rasheed, J. Electroanal. Chem., **857**, 113710 (2020).
14. X. Su, G. Feng, L. Yu, Q. Li, H. Zhang, W. Song and G. Hu, J. Mater. Sci.: Mater. Electron., **30**, 3545 (2019).
15. N. G. Prakash, M. Dhananjaya, A. L. Narayana, D. P. Shaik, P. Rosaiah and O. M. Hussain, Ceram. Int., **44**, 9967 (2018).
16. J. Li, Y. Wang, W. Xu, Y. Wang, B. Zhang, S. Luo, X. Zhou, C. Zhang, X. Gu and C. Hu, Nano Energy, **57**, 379 (2019).
17. K. Panigrahi, P. Howli and K. K. Chattopadhyay, Electrochim. Acta, **337**, 135701 (2020).
18. N. Kumar, A. Juyal, V. Gajraj, S. Upadhyay, N. Priyadarshi, S. Chetana, N. C. Joshi and A. Sen, Inorg. Chem. Commun., **150**, 110439 (2023).
19. S. Zhao, Y. Sun, G. Jia and J. Cui, Mater. Lett., **350**, 134883 (2023).
20. Z. Huang, H. Zeng, L. Xue, X. Zhou, Y. Zhao and Q. Lai, J. Alloys Compd., **509**, 10080 (2011).
21. Y. Chen, P. Lian, J. Feng, Y. Liu, L. Wang, J. Liu and X. Shi, Chem. Eng. J., **429**, 132274 (2022).
22. H. A. Ghaly, A. G. El-Deen, E. R. Souaya and N. K. Allam, Electrochim. Acta, **310**, 58 (2019).
23. Q. Wei, J. Liu, W. Feng, J. Sheng, X. Tian, L. He, Q. An and L. Mai, J. Mater. Chem. A, **3**, 8070 (2015).
24. W. Bi, J. Huang, M. Wang, E. P. Jahrman, G. T. Seidler, J. Wang, Y. Wu, G. Gao, G. Wu and G. Cao, J. Mater. Chem. A, **7**, 17966 (2019).
25. Y. Zhang, X. Yuan, T. Lu, Z. Gong, L. Pan and S. Guo, J. Colloid Interface Sci., **585**, 347 (2021).
26. A. Lazauskas, L. Marcinauskas and M. Andrulevicius, ACS Appl. Mater. Interfaces, **12**, 18877 (2020).
27. A. S. Etman, Z. Wang, Y. Yuan, L. Nyholm and J. Rosen, Energy Technol., **8**, 2000731 (2020).
28. Z. D. Geng and Y. Wang, J. Solid State Electrochem., **19**, 3131 (2015).
29. Y. Fan, Y. Yu, P. Wang, J. Sun, M. Hu, J. Sun, Y. Zhang and C. Huang, J. Colloid Interface Sci., **633**, 333 (2023).
30. K. Dai, L. Lu, C. Liang, J. Dai, Q. Liu, Y. Zhang, G. Zhu and Z. Liu, Electrochim. Acta, **116**, 111 (2014).
31. D. Dhamodharan, P. P. Ghoderao, V. Dhinakaran, S. Mubarak, N. Divakaran and H. S. Byun, J. Ind. Eng. Chem., **106**, 20 (2022).
32. R. Azadvari, S. Mohammadi, A. Habibi, S. Ahmadi and Z. Sanaee, J. Phys. D: Appl. Phys., **57**, 045501 (2023).
33. T. Gao, F. Zhou, W. Ma and H. Li, Electrochim. Acta, **263**, 85 (2018).
34. M. Liu, J. Niu, Z. Zhang, M. Dou and F. Wang, Nano Energy, **51**, 366 (2018).
35. W. Avansi Jr., C. Ribeiro, E. R. Leite and V. R. Mastelaro, Cryst. Growth Des., **9**, 3626 (2009).
36. Z. Feng, Y. Zhang, J. Sun, Y. Liu, H. Jiang, M. Cui, T. Hu and C. Meng, Chem. Eng. J., **433**, 133795 (2022).

37. H. Han, Y. Cheng, C. Fang, T. Zhao, J. Liu and H. Du, ACS Appl. Nano Mater., **6**, 14680 (2023).
38. W. Jiang, J. Ni, K. Yu and Z. Zhu, Appl. Surf. Sci., **257**, 3253 (2011).
39. G. R. Mutta, S. R. Popuri, P. Ruterana and J. Buckman, J. Alloys Compd., **706**, 562 (2017).
40. M. Saini, B. S. Dehiya, A. Umar and M. S. Goyat, Ceram. Int., **45**, 18452 (2019).
41. B. Li, Y. Xu, G. Rong, M. Jing and Y. Xie, Nanotechnology, **17**, 2560 (2006).
42. C. J. Shih, S. Lin, R. Sharma, M. S. Strano and D. Blankschtein, Langmuir, **28**, 235 (2012).
43. H. Liu, Y. Gao, J. Zhou, X. Liu, Z. Chen, C. Cao, H. Luo and M. Kanehira, J. Solid State Chem., **214**, 79 (2014).
44. S. R. Popuri, M. Miclau, A. Artemenko, C. Labrugere, A. Villesuzanne and M. Pollet, Inorg. Chem., **52**, 4780 (2013).
45. T. H. Wu, J. A. Chen and J. H. Su, J. Colloid Interface Sci., **654**, 308 (2023).
46. S. H. Lee, H. M. Cheong, M. J. Seong, P. Liu, C. E. Tracy, A. Mascarenhas, J. R. Pitts and S. K. Deb, Solid State Ionics, **165**, 111 (2003).
47. F. Ureña-Begara, A. Crunteanu and J. P. Raskin, Appl. Surf. Sci., **403**, 717 (2017).
48. N. M. Abd-Alghafour, N. M. Ahmed, Z. Hassan and M. A. Almessiere, J. Phys.: Conf. Ser., **1083**, 012036 (2018).
49. N. M. Abd-Alghafour, G. A. Naeem and S. M. Mohammad, J. Phys.: Conf. Ser., **1535**, 012046 (2020).
50. R. Parmar, D. B. de Freitas Neto, E. Y. Matsubara, R. Gunnella and J. M. Rosolen, Sustainable Energy Fuels, **4**, 3951 (2020).
51. K. Krishnamoorthy, M. Veerapandian, R. Mohan and S. J. Kim, Appl. Phys. A, **106**, 501 (2012).
52. S. S. Nanda, D. K. Yi and K. Kim, Sci. Rep., **6**, 28443 (2016).
53. R. Li, Y. Wang, C. Zhou, C. Wang, X. Ba, Y. Li, X. Huang and J. Liu, Adv. Funct. Mater., **25**, 5384 (2015).
54. S. H. Aboutalebi, A. T. Chidembo, M. Salari, K. Konstantinov, D. Wexler, H. K. Liu and S. X. Dou, Energy Environ. Sci., **4**, 1855 (2011).
55. D. Chen, R. Yi, S. Chen, T. Xu, M. L. Gordin, D. Lv and D. Wang, Mater. Sci. Eng., B, **185**, 7 (2014).
56. M. Fu, Q. Zhuang, Z. Zhu, Z. Zhang, W. Chen, Q. Liu and H. Yu, J. Alloys Compd., **862**, 158006 (2021).

Author Information

Hyegyeong Hwang

Graduate Student, Department of Materials Convergence and System Engineering, Changwon National University

Jinsung Kwak

Professor, Department of Physics & Department of Materials Convergence and System Engineering, Changwon National University